Effect of a high-resolution differencing scheme on finite-volume predictions of viscoelastic flows

M.A. Alves[a], F.T. Pinho[b,*], P.J. Oliveira[c]

[a] *Departamento de Engenharia Química, Faculdade de Engenharia da Universidade do Porto,
Rua dos Bragas, 4050-123 Porto, Portugal*
[b] *Centro de Estudos de Fenómenos de Transporte, DEMEGI, Faculdade de Engenharia da Universidade do Porto,
Rua dos Bragas, 4050-123 Porto, Portugal*
[c] *Departamento de Engenharia Electromecânica, Universidade da Beira Interior, 6200 Covilhã, Portugal*

Abstract

Improved accuracy and enhanced convergence rate are achieved when a finite-volume method (FVM) is used in conjunction with a high-resolution scheme (MINMOD) to represent the stress derivatives in the constitutive equation, because it avoids oscillations of the solution field near sharp stress gradients. Calculations for the benchmark flow of an upper-convected Maxwell fluid through a 4:1 plane contraction were carried out at a constant Reynolds number of 0.01 and varying Deborah numbers in four consistently refined meshes, the finest of which had a normalised cell size of 0.005 in the vicinity of the re-entrant corner. The MINMOD scheme was able to provide converged solutions up to Deborah numbers well beyond those attained by other second-order accurate schemes. The asymptotic behaviour of velocity and stresses near the re-entrant corner was accurately predicted as compared with Hinch's theory [1]. The simulations improved previous results for the same flow conditions obtained with less accurate schemes, and the present results can be used as benchmark values up to a Deborah value of 3 with quantified numerical uncertainties. © 2000 Elsevier Science B.V. All rights reserved.

Keywords: 4:1 Plane contraction; Viscoelastic; Collocated mesh; Finite-volume; Lip vortex; High-resolution scheme; MINMOD; Benchmark flow

1. Introduction

The nineties have seen a renewed interest in finite-volume methods (FVM) to simulate flows of viscoelastic fluids stimulated by their inherent economy of computational resources. Most of those FVM were restricted to orthogonal staggered grids, as in the works of Yoo and Na [2], Sasmal [3] or Xue et al. [4], amongst others. These works relied on first-order upwind differencing schemes (UDS) to represent

---

* Corresponding author.
E-mail addresses: mmalves@fe.up.pt (M.A. Alves), fpinho@fe.up.pt (F.T. Pinho), pjpo@ubi.pt (P.J. Oliveira)

the convective terms but it is known that these schemes may cause severe loss of accuracy whenever the flow is not aligned with the grid.

The need to predict viscoelastic flows in complex geometries has been recently addressed by Huang et al. [5], who used a non-structured method to simulate inertialess flow of Phan-Thien–Tanner (PTT) fluids in eccentric bearings and, in more general terms, a fully collocated FVM was introduced by Oliveira et al. [6] and was extended to handle PTT fluids [7]. This method is based on non-orthogonal block-structured grids with a pressure-correction technique and has been used to predict the slip-stick flow, the flow around a cylinder and high-Deborah number flows in plane contractions. These developments shortened the gap relative to finite-element methods (FEM) as far as the ability to handle complex geometries is concerned.

Regardless of the computational method, improved accuracy requires the use of higher-order differencing schemes (HOS) and/or the use of finer grids. However, when the elasticity of the flow is increased, as measured by the Deborah or Weissenberg numbers, iterative convergence with HOS becomes more difficult to attain and may even preclude the use of finer grids beyond a certain degree of refinement. Besides, use of very fine grids is frequently out of question, especially in complex three-dimensional (3-D) flows, on the ground of memory limitations. In FEM, improvements have been achieved as documented in the work of Rajagopalan et al. [8] and more recently by Matallah et al. [9], but this is still an area of active research and especially so with FVM. The attractiveness of HOS was well exemplified in the work of Oliveira et al. [6] who used the second-order linear upwind interpolation scheme (LUDS) to find improvements in the predictions of the drag coefficient of a cylinder relative to those obtained with the first-order upwind scheme. Mompean and Deville [10] applied the quadratic upwind scheme (QUICK) to represent the convective terms in the momentum and stress equations; this scheme is third-order in regular meshes but reduces to second-order accuracy in irregular grids. Their meshes were orthogonal and staggered, and they were able to achieve converged solutions in a plane 4:1 sudden contraction flow of an Oldroyd-B fluid up to a Deborah number of 9.1 but their finest grid was rather coarse (their smallest normalised spacing was larger than 0.05).

An analysis of the advantages and shortcomings of using the LUDS was recently carried out by Oliveira and Pinho [7] who computed the flow of upper-convected Maxwell fluids (UCM) in a 4:1 plane contraction for increasing Deborah numbers and three consecutively refined meshes. The need for very stringent assessment of grid dependence is especially important in viscoelastic flows, as found by Coates et al. [11], because the resolution of the stress fields around geometrical singularities tends to require finer grids than the equivalent inelastic flows. LUDS was shown [7] to lead to improved predictions compared to UDS, but failed to converge at rather low values of the Deborah number when the computational meshes are fine (De=2). Those convergence problems have been traced back by Oliveira and Pinho [7] to a lack of delimiters in the HOS formulation with the consequence that, in regions of high stress gradients, stress values at cell faces can be much higher than the values at the neighbouring nodes. A solution to this problem is the enforcement of adequate boundedness criteria everywhere in the flow field, and especially in those regions with high stress gradients. The convection boundedness criterion of Gaskell and Lau [12] is one such method which avoids oscillations of the solution field. When coupled with a set of HOS, the resulting combination produces the so-called high-resolution schemes, one such example being the MINMOD scheme introduced by Harten [13]. Use of non-uniform finite-volume meshes are required to solve those sharp gradients, but they pose no problem if the normalised variable and space formulation of Darwish and Moukalled [14] is adopted.

Although simple from a purely geometric point of view, the 4:1 plane contraction flow gives rise to locally complex flows that are difficult to predict numerically because of the high stress gradients found in

the vicinity of the re-entrant corner, and therefore constitutes a common benchmark to develop/improve numerical methods. A recent review of the experimental and numerical characteristics of this flow can be found in Oliveira and Pinho [7].

It is the objective of this work to improve the accuracy of the predictions obtained with the FVM of Oliveira and Pinho [7] by introducing a high-resolution scheme to represent the convective terms in the stress equations. This practice will be assessed from results of calculations of the flow of a UCM fluid in a 4:1 contraction using four consecutively refined meshes (the same three meshes used in [7], plus a fourth finer grid with half the cell size). In this way we are able to determine the extent of Deborah numbers over which there is a consistent and accurate prediction of some flow characteristics, like the size and strength of the vortices formed upstream of the contraction. These benchmark data is missing in the literature for this so-called benchmark problem of the flow through the 4:1 planar contraction which turns out to be much more interesting than anticipated.

This paper is organised as follows: the equations to be solved are presented in Section 2 and the numerical method is outlined in Section 3 with emphasis given to the implementation of the high-resolution scheme. The flow configuration and computational meshes are described in Section 4 and the results of the calculations and their discussions are given in Section 5. The paper ends with a summary of the main conclusions.

2. Governing equations

The basic equations to be solved are those for 2-D or 3-D, incompressible and isothermal laminar flow of an UCM fluid. In the Cartesian tensor notation, they are the continuity equation

$$\frac{\partial u_i}{\partial x_i} = 0, \tag{1}$$

the equation for conservation of linear momentum

$$\frac{\partial \rho u_i}{\partial t} + \frac{\partial \rho u_j u_i}{\partial x_j} = -\frac{\partial p}{\partial x_i} + \frac{\partial \tau_{ij}}{\partial x_j} \tag{2}$$

and the constitutive equation for the extra stress tensor τ_{ij} [15]

$$\tau_{ij} + \lambda \left(\frac{\partial \tau_{ij}}{\partial t} + \frac{\partial u_k \tau_{ij}}{\partial x_k} \right) = \lambda \left(\tau_{ik} \frac{\partial u_j}{\partial x_k} + \tau_{jk} \frac{\partial u_i}{\partial x_k} \right) + \eta \left(\frac{\partial u_i}{\partial x_j} + \frac{\partial u_j}{\partial x_i} \right). \tag{3}$$

In the equations, u_i is the velocity component along the Cartesian co-ordinate x_i, ρ the fluid density, p the pressure, η the shear viscosity and λ the relaxation time. The terms on the left-hand side of Eqs. (2) and (3) will be dealt with implicitly, while those on the right-hand side go into the source term of the matrix equations resulting from the discretisation procedure. The UCM equation is one of the simplest models to represent viscoelastic fluid behaviour, but also one of the most challenging from the numerical point of view because it tends to develop the highest stress growth-rate near singularities of all constitutive models.

3. Finite-volume numerical method

The numerical method is only briefly outlined below as it has been described in detail in Oliveira et al. [6]. Here, the focus is on the implementation of the high-resolution scheme in the constitutive equation.

The conservation and constitutive equations given in Section 2 are transformed into a general non-orthogonal co-ordinate system. The transformation is required for easy application of our FVM based on the collocated mesh arrangement, and the equations are then integrated over a set of non-overlapping control volumes (cells).

The dependent variables remain the three Cartesian velocity components, the pressure, and the six Cartesian stress components, which are all stored at the centre of the cells as implied by the present non-staggered computational mesh. To avoid pressure–velocity and stress–velocity decoupling, a special procedure explained in the previous works [6,16] is adopted here.

3.1. Continuity equation

The discretised form of the continuity Eq. (1) is

$$\sum_{f=1}^{6} F_f = 0, \tag{4}$$

where F_f are the outgoing mass flow rates across a face f of any cell in the computational mesh. In order to ensure an adequate coupling between the velocity and pressure fields, a special Rhie-and-Chow type of interpolation is used to evaluate the velocity components at a cell face [17], which is required for the calculation of the fluxes F_f. The precise form is given in [18].

3.2. Momentum equation

The discretised form of the momentum equation (Eq. (2)), after integration over a general cell P with volume V_P, can be cast under the common linearised form

$$a_P u_{i,P} - \sum_F a_F u_{i,F} = S_{u_i} + \frac{\rho V_P}{\delta t} u_{i,P}^{(n)}, \tag{5}$$

where δt is the time step, $u_{i,P}^{(n)}$ denotes the velocity at the previous time level and a_F are coefficients accounting for flux interactions with the neighbour cells, F spanning the near-neighbouring cells of P. At this stage, the a_F are composed of convective contributions only ($a_F = a_F^C$) since there is no explicit diffusion term in the original momentum (Eq. (2)). These convective coefficients are given by

$$a_F^C = -\min(F_f, 0), \tag{6}$$

an expression valid for the upwind scheme while for the higher-order schemes additional terms arise which are incorporated into the source term as described in [6]. The central coefficient in Eq. (5) is

$$a_P = \frac{\rho V_P}{\delta t} + \sum_F a_F \tag{7}$$

and the source term S_{u_i} encompasses all contributions not included elsewhere, which are, from inspection of Eq. (2), given by

$$S_{u_i} = S_{u_i\text{-pressure}} + S_{u_i\text{-stress}}. \tag{8}$$

Particular attention must be paid to the stress term resulting from the action of the stress tensor on all surface faces of any given cell

$$S_{u_i\text{-stress}} = \sum_{f=1}^{6}\sum_{j=1}^{3} B_{fj}(\tilde{\tau}_{ij})_f, \tag{9}$$

where B_{fj} are cell-face area components and the cell-face stresses $\tilde{\tau}_{ij}$ should follow the interpolation methods introduced in [6] and [16].

3.2.1. Addition of explicit diffusion term

In order to promote numerical stability and also for the method to be valid even for creeping flow conditions (in which case the $a_F^C = 0$), we follow the practice of [6] of adding and subtracting a diffusive term to Eq. (5). Thus,

$$a_P^C u_{i,P} - \sum_F a_F^C u_{i,F} = S_{u_i} + \frac{\rho V_P}{\delta t} u_{i,P}^{(n)} + \underbrace{\sum_F a_F^D (u_{i,F} - u_{i,P})}_{\text{implicit diffusive flux}} - \underbrace{\sum_F a_F^D (u_{i,F}^{(n)} - u_{i,P}^{(n)})}_{\text{explicit diffusive flux}} \tag{10}$$

with the diffusion coefficient given by

$$a_F^D = \frac{\eta_f B_f^2}{V_f}, \tag{11}$$

where B_f is the scalar cell-face area and V_f is the volume of a pseudocell centered at the face. It is already clear from Eq. (10) that we decided to treat differently the two parts of the new term: the first will be treated implicitly, so the u_i are evaluated at the new time-level; the second part is treated explicitly with $u_i^{(n)}$ at the previous time-level. If now we regroup the different terms in Eq. (10), the coefficients being now

$$a_F = a_F^C + a_F^D \tag{12}$$

and the new source term becoming (with S_{u_i} from Eq. (8))

$$S_{u_i} = S_{u_i} - \sum_F a_F^D (u_{i,F}^{(n)} - u_{i,P}^{(n)}), \tag{13}$$

we recover the discretised momentum equation (Eq. (5)).

A few comments are necessary regarding this practice. Firstly, it should be clear that this practice does not introduce any numerical diffusion and does not affect the final, steady state solution. Indeed, if we look at Eq. (10) we see that as the steady solution is reached $u_i^{(n)} \to u_i$, the added terms cancel out exactly, and we are therefore solving the original Eq. (5) without explicit diffusion terms. The time-advancement path to the steady-state is, however, affected by this practice, but even here the truncation error introduced

is of the same order of the error associated with the discretisation in time ($O(\delta t)$, for implicit Euler scheme). In this respect, the practice is similar to the factored-time advancement practices so common in finite-difference methods.

Secondly, the practice can also be viewed as a partial application of EVSS [8] and is, in fact, not new. It was applied in the early finite-difference methods in computational rheology by Perera and Walters [19] and was later re-invented by Guénnette and Fortin [20] in the context of FEM. The key point of EVSS is to split the stress tensor into elastic and viscous components, $\boldsymbol{\tau}=\boldsymbol{\tau}_1+\boldsymbol{\tau}_2$, with $\boldsymbol{\tau}_2=2\eta\boldsymbol{D}$, to obtain a momentum equation (in compact form):

$$\rho\frac{\mathrm{D}\boldsymbol{u}}{\mathrm{D}t} = -\nabla p + \nabla\cdot\boldsymbol{\tau}_1 + \eta\nabla^2\boldsymbol{u}. \tag{14}$$

Now, instead of doing the same substitution in the constitutive Eq. (3), we find it better (as Guénnette and Fortin did) to keep τ as the main dependent variable there, and consequently replace $\tau_1=\tau-\tau_2$ in the above momentum equation, to obtain

$$\rho\frac{\mathrm{D}\boldsymbol{u}}{\mathrm{D}t} = -\nabla p + \nabla\cdot\boldsymbol{\tau} + \eta\nabla^2\boldsymbol{u} - \eta\nabla^2\boldsymbol{u}, \tag{15}$$

which is exactly the equation we are solving for. The advantage is that any constitutive equation can be dealt with similarly (not only the UCM), and we avoid evaluation and storage of the Oldroyd derivative of D.

3.3. Constitutive equation

The UCM constitutive equation (Eq. (3)) is likewise transformed from differential to finite-volume form after integration over a general cell P, to give an algebraic equation with similar linearised structure as the momentum equations beforehand

$$a_{\mathrm{P}}^{\tau}\tau_{ij,\mathrm{P}} - \sum_F a_F^{\tau}\tau_{ij,F} = S_{\tau_{ij}} + \frac{\lambda V_{\mathrm{P}}}{\delta t}\tau_{ij,\mathrm{P}}^{(n)}. \tag{16}$$

It is noted that, however, since there is no diffusive term in the original stress equation, the coefficients a_F^{τ} are composed only by convective contributions, which in the simpler case of using the UDS are given by

$$a_F^{\tau} = \frac{\lambda}{\rho}a_F^{\mathrm{C}}, \tag{17}$$

with a_F^{C} from Eq. (6), and the central coefficient is then

$$a_{\mathrm{P}}^{\tau} = V_{\mathrm{P}} + \sum_F a_F^{\tau} + \frac{\lambda V_{\mathrm{P}}}{\delta t}. \tag{18}$$

A manipulation like that explained above for the momentum equation is not deemed necessary.

The source term in Eq. (16), in addition to incorporating part of the Oldroyd derivatives from Eq. (3) which are evaluated with the use of central differences, also includes additional terms due to use of high-order or high-resolution schemes in the evaluation of the convective terms. These issues are pivotal to the present study and are discussed hereafter.
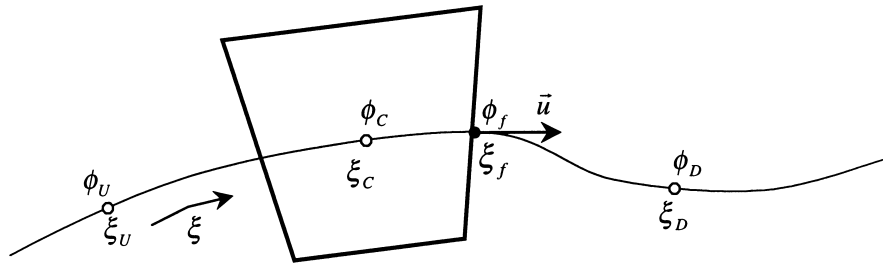
Fig. 1. Definition of local variables and co-ordinate system.

3.4. High-resolution differencing schemes

Our previous work [6,7,16] has shown that the use of HOS can significantly improve the accuracy of the numerical solutions but has also shown that these schemes suffer from convergence difficulties and a strong tendency for oscillations and overshoots, especially in regions with sharp gradients of the variables [21]. To remedy these shortcomings, a number of composite bounded higher-order schemes (usually known as high-resolution schemes) have been proposed and unified within the context of the normalised variable and space formulation (NVSF) of Darwish and Moukalled [14].

According to this NVSF methodology the convected variable ϕ (which can be any of the stress components τ_{ij}) and the general curvilinear co-ordinate ξ, shown schematically in Fig. 1, are normalised as

$$\widehat{\phi} = \frac{\phi - \phi_{\mathrm{U}}}{\phi_{\mathrm{D}} - \phi_{\mathrm{U}}}, \tag{19}$$

$$\widehat{\xi} = \frac{\xi - \xi_{\mathrm{U}}}{\xi_{\mathrm{D}} - \xi_{\mathrm{U}}}, \tag{20}$$

where the subscripts U and D refer to the upstream and downstream cells to cell C which is, itself, upstream of the cell face f under consideration.

In order to satisfy the convection boundedness criterion (CBC) of Gaskell and Lau [12] the functional relationship of an interpolation scheme applied to a cell face f, $\widehat{\phi}_f = \Omega(\widehat{\phi}_{\mathrm{C}})$, must be continuous and bounded from below by $\widehat{\phi}_f = \widehat{\phi}_{\mathrm{C}}$ and from above by unity, in the monotonic range $0 < \widehat{\phi}_{\mathrm{C}} < 1$. For the ranges $\widehat{\phi}_{\mathrm{C}} \leq 0$ and $\widehat{\phi}_{\mathrm{C}} \geq 1$, the function $\Omega(\widehat{\phi}_{\mathrm{C}})$ must equal $\widehat{\phi}_{\mathrm{C}}$. This notion of CBC can be illustrated on a normalised variable diagram (NVD) as shown in Fig. 2 by the shadowed area together with the line with slope 1 outside that area. The various straight lines in this figure are for the UDS, the LUDS and the CDS (central differencing) schemes, as can be easily inferred (see e.g. Darwish and Moukalled [14]).

Fig. 2 shows that the lines representing the second-order LUDS and CDS schemes do not completely satisfy the CBC criterion in the whole range, but it is possible to combine them into a composite high-resolution (HR) scheme which satisfies the CBC criterion. The particular combination seen in Fig. 2 is the MINMOD scheme of Harten [13] and can be expressed analytically, using the NVSF formulation [14], as
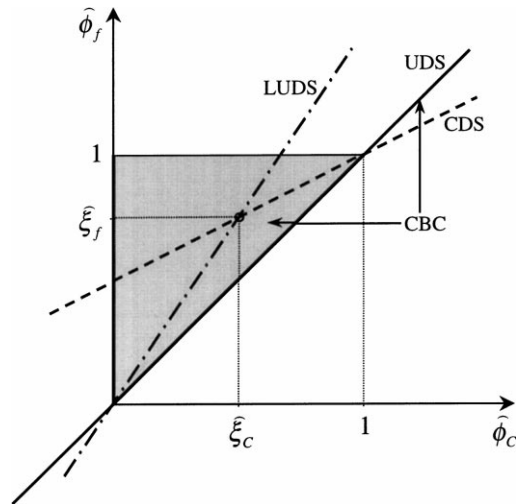
Fig. 2. Normalised variable diagram (NVD) for different interpolating schemes showing the convective boundedness criterion (CBC). (Differencing schemes: UDS≡upwind, LUDS≡linear upwind, CDS≡central).

$$
\widehat{\phi}_f = \begin{cases}
\dfrac{\widehat{\xi}_f}{\widehat{\xi}_C}\widehat{\phi}_C & 0 < \widehat{\phi}_C < \widehat{\xi}_C \quad \text{(LUDS)}, \\[3mm]
\dfrac{1-\widehat{\xi}_f}{1-\widehat{\xi}_C}\widehat{\phi}_C + \dfrac{\widehat{\xi}_f-\widehat{\xi}_C}{1-\widehat{\xi}_C} & \widehat{\xi}_C \le \widehat{\phi}_C < 1 \quad \text{(CDS)}, \\[3mm]
\widehat{\phi}_C & \text{elsewhere} \qquad \text{(UDS)}.
\end{cases}
\tag{21}
$$

It is computationally advantageous to express Eq. (21) as a combination of linear relationships of the form

$$
\widehat{\phi}_f = a + b\widehat{\phi}_C,
\tag{22}
$$

which can be transformed into Eq. (23) after some algebra and the use of the normalised variables defined by Eq. (19)

$$
\phi_f = \phi_C + a(\phi_D - \phi_U) + (b - 1)(\phi_C - \phi_U).
\tag{23}
$$

When the MINMOD method is applied to the convective fluxes in the stress equation, these become, at any cell face f:

$$
\frac{\lambda}{\rho}F_f\hat{\tau}_{ij,f} = \frac{\lambda}{\rho}F_f[\tau_{ij,C} + a(\tau_{ij,D} - \tau_{ij,U}) + (b-1)(\tau_{ij,C} - \tau_{ij,U})]_f,
\tag{24}
$$

or, alternatively,

$$
\frac{\lambda}{\rho}F_f\hat{\tau}_{ij,f} = \frac{\lambda}{\rho}F_f\tau_{ij,C} + \frac{\lambda}{\rho}F_f[a(\tau_{ij,D} - \tau_{ij,U}) + (b-1)(\tau_{ij,C} - \tau_{ij,U})]_f.
\tag{25}
$$

With the fluxes written under this form, we recognise the first term on the right-hand side of Eq. (25) as being the flux for the upwind scheme (compare with Eq. (17)) while the term in square brackets arises from the HR scheme.

In spite of its disadvantages regarding accuracy, the UDS scheme possesses an inherent stability advantage, which can be used to profit in the deferred correction approach [22]. With the deferred correction, a higher-order or high-resolution scheme can be easily implemented into a numerical procedure designed for the upwind scheme. The coefficients of the discretised stress equations are kept as those for the UDS, thus the a_F^τ are still given by Eq. (17) and contain the first part of the flux (25); the remaining part of (25) is inserted into the source terms, the $S_{\tau_{ij}}$ in Eq. (16), and is thus treated explicitly in the context of the time advancement. While this explicit addition of some of the convective flux terms may lead to a relative slowdown of the iterative-like procedure, the simplicity of implementation of the deferred correction approach together with the important memory-saving fact that the coefficients a_F^τ and a_P^τ are then the same for all the six stress equations, make this approach very appealing and it is thus adopted here.

3.5. Solution procedure

The sets of discretised equations for each variable are solved in a sequential manner and the SIMPLEC algorithm of Van Doormal and Raithby [23] is used to handle the pressure–velocity coupling. Since the original algorithm is mainly concerned with the way to obtain a pressure field that satisfies the continuity constraint, its extension to viscoelastic flows is marginally affected by the presence of a different constitutive equation. The revised version of the SIMPLEC algorithm used in the calculations was explained in [6] and consists of the following steps to advance the solution from time level (*n*) to (*n*+1).

1. Solve Eq. (26) to obtain updated values of cell-centred stresses, $\tau_{ij,P}^*$:

$$a_P^\tau \tau_{ij,P}^* = \sum_F a_F^\tau \tau_{ij,F}^* + S_{\tau_{ij}}^{(n)} + \frac{\lambda V_P}{\delta t} \tau_{ij,P}^{(n)}, \tag{26}$$

   where the coefficients, the source term and the inertia term are obtained from previous time level velocity and stress values. Compute the cell-face stresses required in the divergence term in the momentum equations, $\tilde{\tau}_{ij,f}$ in Eq. (9), using the special interpolation described in [6] or [16] which precludes stress–velocity decoupling.

2. Solve the momentum equations implicitly for each velocity component, u_i^*:

$$a_P u_{i,P}^* = \sum_F a_F u_{i,F}^* + S_{u_i}^{(n)} + \frac{\rho V_P}{\delta t} u_{i,P}^{(n)}, \tag{27}$$

   where the calculated velocity components at this intermediate level, u_i^*, do not generally satisfy the continuity equation. The next step of the algorithm involves a correction to u_i^*, and to the pressure field p^* embedded into the pressure-gradient terms in S_{u_i}, so that the updated velocity field u_i^{**} and the corrected pressure field p^{**} will satisfy simultaneously the momentum and continuity equations, as described in detail in [18].

3. Check for iterative convergence to a steady state. Two criteria have been used to stop the time stepping procedure: either the L_1-norm of the residuals of the equations is required to fall below a tolerance of 10^{-4}, or the relative change of the solution satisfies

$$\frac{||X^{(n+1)} - X^{(n)}||_2}{||X^{(n+1)}||_2} \leq \delta, \tag{28}$$

where $X^{(n)}$ is the solution vector at time step (n) and δ a small parameter (typically 10^{-6}–10^{-7}). If convergence is not attained take the variables as pertaining to a new time level $(n+1)$ and go back to step 1.

Implicit solution of the linear set of equations was carried out using standard pre-conditioned conjugate gradient methods [24]. More details of the numerical method, such as the implementation of boundary conditions, can be found in Oliveira et al. [6]. It is noted that with this method we can simulate time-dependent flows with a truncation error of order $O(\delta t)$ in time.

4. Flow geometry and computational mesh

In this work we used as a test case the popular benchmark flow through a 4:1 planar contraction, as sketched in Fig. 3. The figure defines the co-ordinate system, some of the relevant nomenclature and shows the five structured blocks used to generate the four consecutively refined meshes used.

The computational meshes are orthogonal but non-uniform, with increased concentration of cells near the re-entrant corner and the upstream wall where the stress gradients are expected to be higher. In previous work [7,16] it was found that a computational domain extending from $x=-20H_2$ to $x=50H_2$ is appropriate for the present problem. The Reynolds and Deborah numbers are defined on the basis of downstream quantities as

$$Re = \frac{\rho U_2 H_2}{\eta}, \tag{29}$$

$$De = \frac{\lambda U_2}{H_2}, \tag{30}$$

and Re was fixed at 0.01 (representative of creeping flow) while De was varied. Table 1 summarises the main characteristics of the four meshes used in calculations.
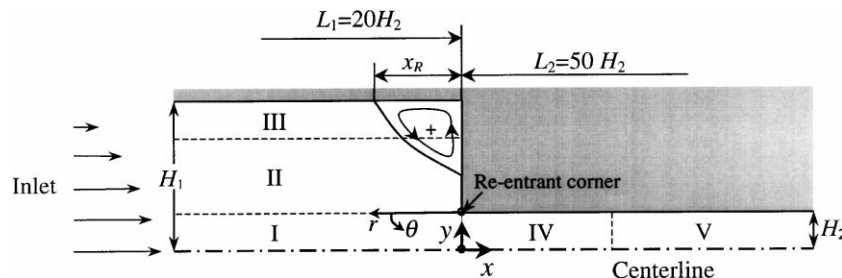

Fig. 3. Schematic representation of the 4:1 planar contraction.

Table 1
Mesh characteristics (domain length is $L_1 = 20H_2$ and $L_2 = 50H_2$)

	Mesh 1			Mesh 2			Mesh 3			Mesh 4		
	NX×NY	f_x	f_y	NX×NY	f_x	f_y	NX×NY	f_x	f_y	NX×NY	f_x	f_y
Block I	24×10	0.8210	0.8475	47×20	0.9061	0.9206	94×40	0.9519	0.9595	188×80	0.9756	0.9795
Block II	24×13	0.8210	1.2091	47×25	0.9061	1.0996	94×50	0.9519	1.0486	188×100	0.9756	1.0240
Block III	24×5	0.8210	0.7384	47×9	0.9061	0.8593	94×17	0.9519	0.9270	188×34	0.9756	0.9628
Block IV	20×10	1.2179	0.8475	40×20	1.1036	0.9206	80×40	1.0505	0.9595	160×80	1.0249	0.9795
Block V	7×10	1.3782	0.8475	13×20	1.1740	0.9206	25×40	1.0835	0.9595	50×80	1.0409	0.9795
NC	942			3598			14258			57032		
	$\delta x_{min} = \delta y_{min}$ $= 0.04H_2$			$\delta x_{min} = \delta y_{min}$ $= 0.02H_2$			$\delta x_{min} = \delta y_{min}$ $= 0.01H_2$			$\delta x_{min} = \delta y_{min}$ $= 0.005H_2$		

The cell size inside each of the five blocks used in a given mesh varied in geometrical progression at a constant ratio, defined as $f_x \equiv \delta x_{i+1}/\delta x_i$, where δx_i is the i-cell size in the x-direction. In order to guarantee a smooth cell-size variation inside and in-between the patched sub-blocks the contraction factors were chosen to be near unity for the finest meshes. During mesh refinement the number of cells along each direction was doubled, and the corresponding expansion/contraction ratios (f_x and f_y) inside each sub-block were root-squared. This procedure ensured a consistent mesh refinement, with the grid spacing being approximately halved between consecutive meshes, thus enabling error estimation using Richardson's extrapolation to the limit [25]. We emphasise, from the values in Table 1, the large number of cells (NC) used in Meshes 3 and 4.

In particular, Mesh 4 shown partially in Fig. 4 is probably the finest mesh used so far in this benchmark problem (see Table 1 of [7]) with a total of 57 032 cells for a 2-D configuration and a minimum non-dimensional cell size of only 0.005 in both the x- and y-directions near the re-entrant corner $((\delta x/H_2)_{min}$ and $(\delta y/H_2)_{min})$. One of the finite-element meshes used by Coates et al. [11] in the corresponding axisymmetric problem had similar minimum cell size but the total number of elements (cells) was much less, by more than one order of magnitude. The higher-order interpolation polynomials used by [11] (biquadratic for velocity and stresses and bilinear for pressure) can in part compensate for less refined meshes, but the vortex activity and size cannot be properly predicted if the mesh does not possess a convenient level of refinement, at least up to the detachment point. These very refined meshes, in combination with the high-resolution scheme, should allow us to obtain very accurate solutions.

Most computations reported below have been carried out in a PC with a Pentium III processor at 500 MHz, with 128MB core memory. The memory requirements vary broadly with the number of cells in the mesh, the 3-D code requiring 11 arrays to store the dependent variables, seven arrays to store the geometry, 14 integer arrays with connectivities, and 22 arrays for workspace. Thus, for the NC given in Table 1 and accounting (by default) for double-precision storage for all real variables (8B per word), we arrive at a required memory storage of 0.34MB for Mesh 1, 1.3MB for Mesh 2, 5.1MB for Mesh 3 and 20MB for Mesh 4.

The run times varied with the mesh and Deborah number, the initial fields and also with the discretisation scheme. In most cases, we would restart a given run from a converged solution at a De immediately below. An average figure for the specific CPU time was 0.08 ms per time step and per number of cells, using the
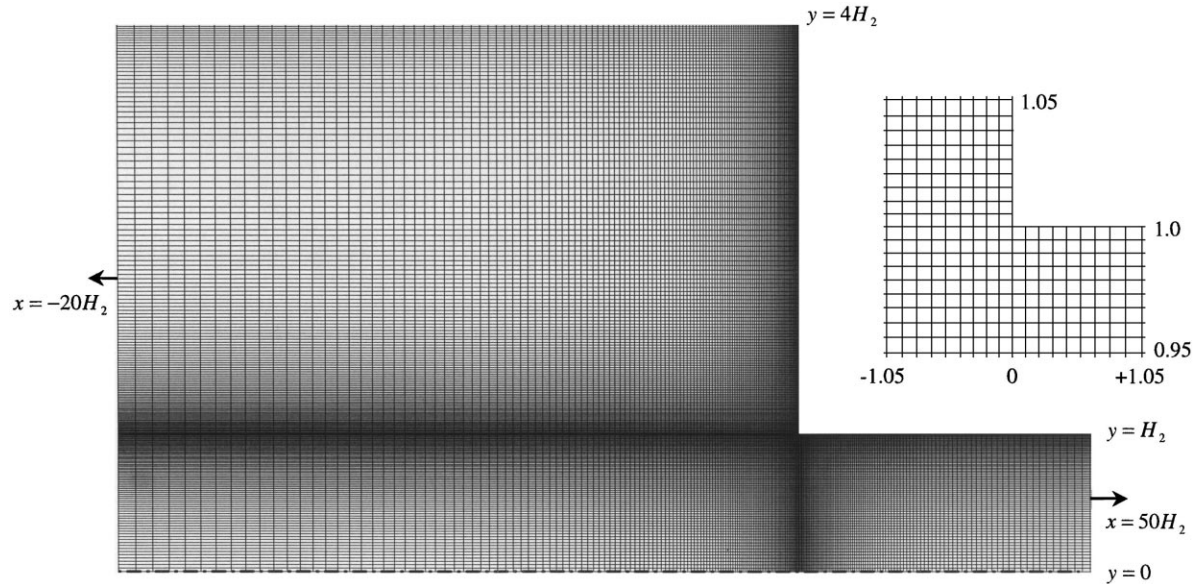
Fig. 4. Zoomed view of the finest mesh used in the calculations (Mesh 4).

UDS scheme. Typical run times for the case De=3 were 30 min in Mesh 1, 4 h in Mesh 2, 34 h in Mesh 3 and a few days in Mesh 4. For the MINMOD scheme, the specific CPU times are approximately 30% higher.

5. Results

Our FVM was applied to the simulation of the plane contraction flow, using the four meshes of Table 1, and the main purpose was to investigate the effects of mesh fineness and differencing scheme on the following characteristics:
1. Asymptotic behaviour near the re-entrant corner singularity.
2. Corner and lip vortex size and strength (establish benchmark results).
3. Distribution of velocities, pressure and stresses along the centerline and downstream channel wall.
4. Stress fields near the singularity.
5. Pressure drop through the contraction (Couette correction).

5.1. Asymptotic behaviour near the re-entrant corner

For Newtonian flows, Dean and Montagnon [26] and Moffatt [27] derived asymptotic expressions for the variation of pressure, velocity and stress components near the re-entrant corner, of the form

$$u_i \propto r^{0.545}, \qquad p, \tau_{ij} \propto r^{-0.455}, \tag{31}$$

for any given angle θ in the polar co-ordinates (r, θ) centred in the corner, as defined in Fig. 3. In Fig. 5 we present the results obtained for a Newtonian fluid at $\theta = \pi/2$ and for creeping flow conditions (Re=0.01).
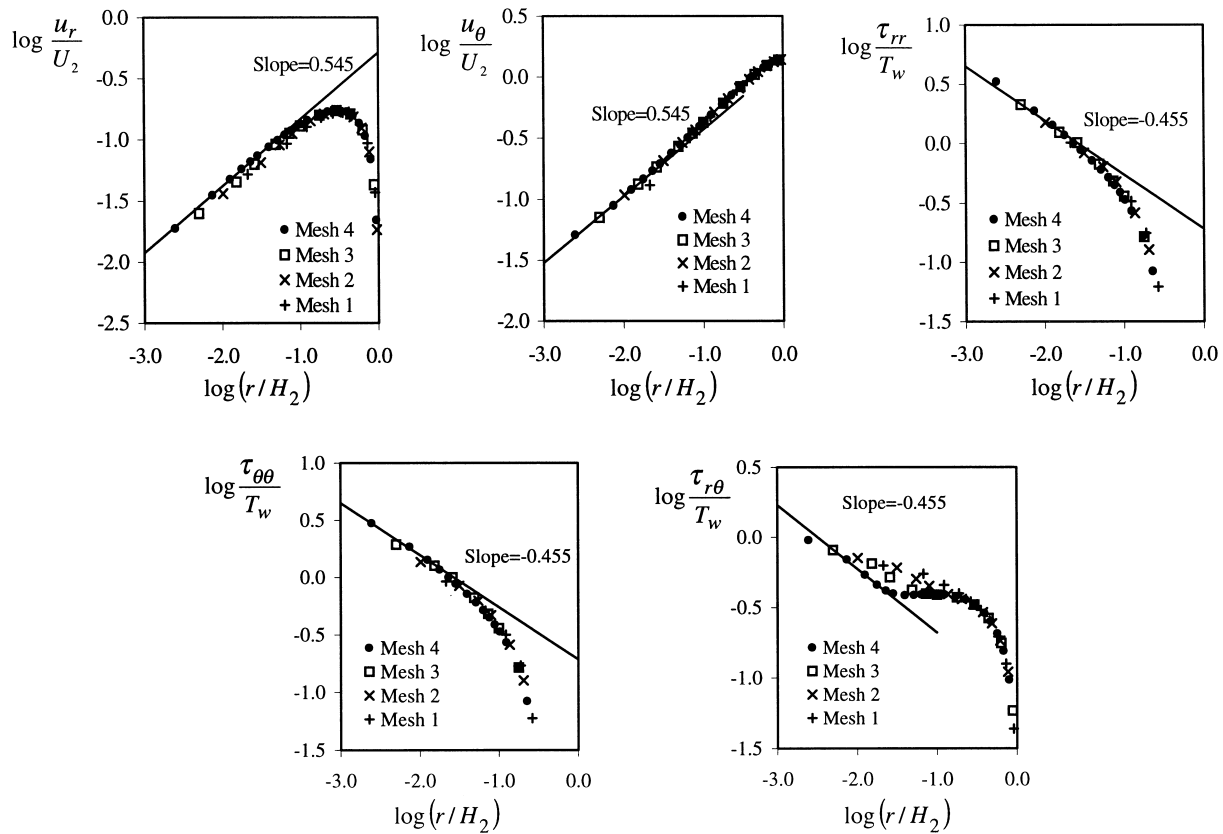
Fig. 5. Asymptotic behaviour of the predicted velocity and stress components near the re-entrant corner, for a Newtonian fluid along direction $\theta = \pi/2$.

The asymptotic behaviour is well captured in all the four meshes except for the $\tau_{r,\theta}$-component, which shows some slight deviations in the coarser meshes, thus giving support to the use of fine meshes even in Newtonian calculations.

For viscoelastic flows obeying the Oldroyd-B constitutive model, Hinch's analysis [1] provides the following asymptotic behaviour in the vicinity of the corner

$$u_i \propto r^{5/9}, \qquad \tau_{ij} \propto r^{-2/3}, \tag{32}$$

for De values below unity. Hinch has pointed out that the results expressed by Eq. (32) result from a domination of the elastic stresses over the solvent viscous stresses hence they are valid for a UCM model, as it is the case here. Numerical calculations with the MINMOD scheme were performed in the four meshes at De=1.0. Higher values of De should not be considered since a significant lip vortex is then seen to develop and the conditions for the applicability of Hinch's analysis are no longer valid. The results of our calculations are shown in Fig. 6 where the asymptotic behaviour of various quantities near the corner at $\theta = \pi/2$ are plotted together with the theoretical asymptotes of Hinch. The agreement is good in all cases for the velocity components and less good for the stress components when these are based on
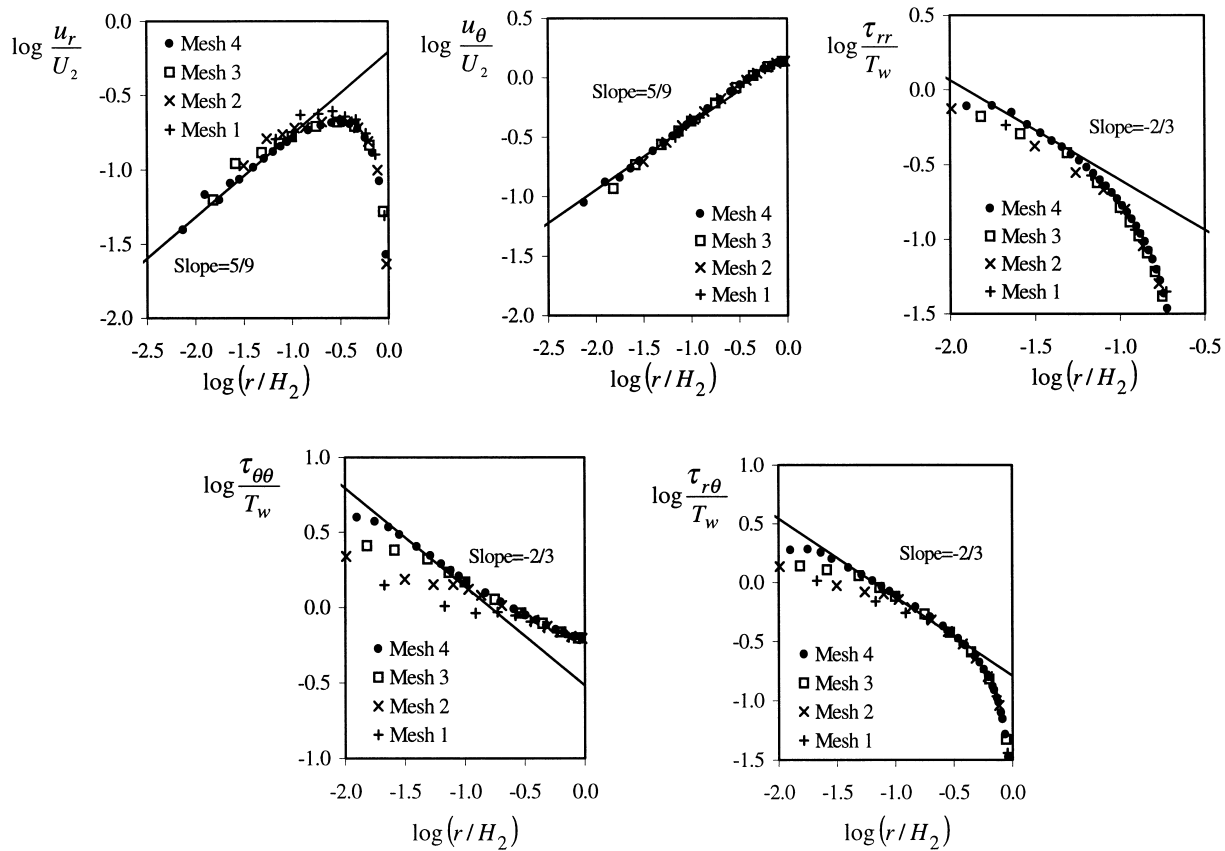
Fig. 6. Asymptotic behaviour of the predicted velocity and stress components near the re-entrant corner, for a viscoelastic fluid at De=1, along direction $\theta = \pi/2$.

the coarsest meshes. However, the predicted asymptotic stress behaviour follows Hinch's analysis quite well when fine meshes are used, a feature especially clear for $\tau_{\theta\theta}$.

The deviation just next to the wall is not unexpected since the 2/3 stress growth predicted by Hinch is only valid in a core region away from the walls. Furthermore, numerical inaccuracies tend to be higher there due to the necessity of reverting locally from second-order central differences to first-order one-sided differences. These unavoidable inconsistencies are magnified near the singular re-entrant corner, on account of the very high gradients, and this is reflected in some oscillations just seen in a few profiles in Fig. 6. Similar or more intense oscillations are seen in most asymptotic plots reported in the literature (cf. Figs. 5, 15 and 16 in [3], Fig. 9 in [11], Figs. 8–11 in [28], Figs. 8, 12 and 13 in [29] and Figs. 5 and 6 in [30]).

5.2. Flow pattern and corner and lip vortex size and strength

Here the focus is on the flow patterns predicted in the different meshes, as a function of the Deborah number and when different interpolating schemes are used for the convective terms in the constitutive

equation. For Newtonian fluids, all tested schemes, namely UDS, LUDS, CDS and MINMOD, induce good convergence behaviour irrespective of mesh fineness. For viscoelastic flow, converged solutions up to a Deborah number of 10 could be obtained only with the first-order UDS, as reported in a previous work [7]. In this work, it was found that the second-order CDS is unstable except for Newtonian fluids. The nominally second-order LUDS scheme was stable only at moderate values of De and the maximum attainable Deborah number was found to decrease with increasing mesh refinement.

The implementation of the high-resolution MINMOD scheme improved accuracy of the solution and extended the range of attainable De, with some limitations discussed below. Irrespective of the scheme used, with the finest Mesh 4 the iterative convergence was rather slow, and for Deborah numbers above 3 the residuals obtained during the iterative procedure with the MINMOD scheme failed to meet both prescribed convergence criteria, probably due to switching between the various differencing schemes
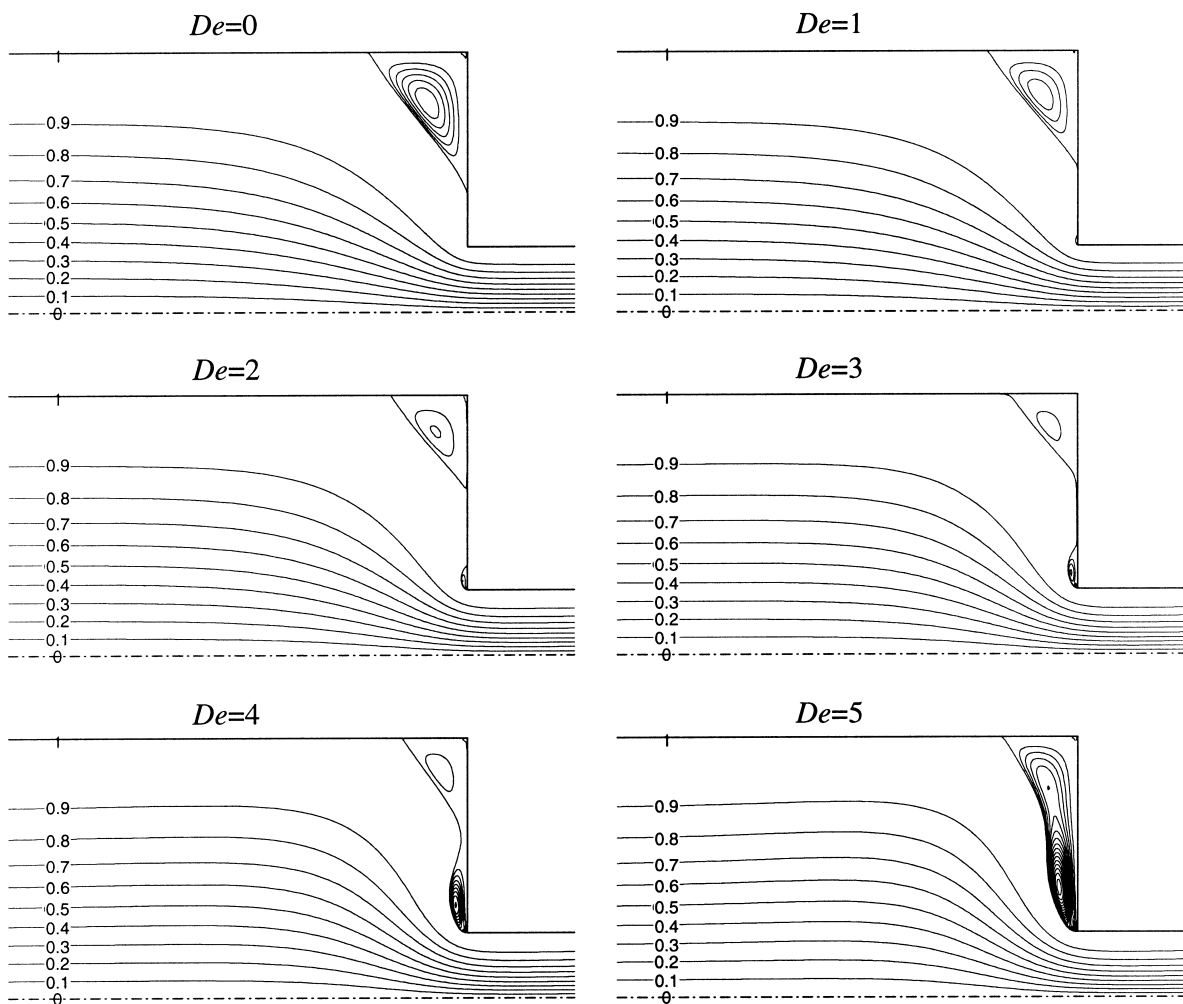

Fig. 7. Sequence of predicted streamlines, obtained with Mesh 3 and the MINMOD scheme, for increasing Deborah numbers at Re=0.01. The streamlines inside vortices are equally spaced, with $\delta_\Psi = 2 \times 10^{-4}$.

within MINMOD. A similar behaviour takes place with coarser meshes at very high De. For Mesh 3 the MINMOD scheme produced converged solutions up to De=5, while with Meshes 1 and 2 convergence was attained up to De=7. This represents a considerable improvement over the attainable De range of the previous work [7].

Fig. 7 presents the streamlines obtained in Mesh 3 with the MINMOD scheme for a range of De from 0 up to 5. The plots confirm the trends reported in [7], based on calculations with the LUDS scheme, and extend the validity of those results to higher Deborah numbers with improved accuracy. There is a significant decrease in both size (of 38%) and intensity (83%) of the salient corner vortex as fluid elasticity is being raised, up to De=3, followed by vortex enhancement for higher De. The corner vortex size is measured by its non-dimensional length, $X_R = x_R/H_2$, and the intensity is calculated by the amount of recirculating flow normalised by the inlet flow rate,

$$\Psi_R = \frac{\psi_R}{U_1 H_1} - 1 \tag{33}$$

In Fig. 7 the streamlines inside the vortices are equally spaced, with constant $\delta_\Psi = 2 \times 10^{-4}$, in order to illustrate vortex intensity and to allow comparison between the various situations. As can be seen, a very small lip vortex extending over a few cells is already present at De=1. This lip vortex increases in size and strength with the Deborah number, gradually approaching the corner vortex with which it eventually merges to become dominant. At a Deborah number of 5 the merging process is practically

Table 2
Dimensionless length of primary vortex (X_R) as a function of Deborah number, mesh and interpolating scheme

De	Scheme	Mesh 1	Mesh 2	Mesh 3	Mesh 4	Extrapolated	Difference (%)[a]
0	CDS	1.470	1.488	1.494	1.495	1.496	0.1
	MINMOD	1.472	1.488	1.494	1.495	1.496	0.1
1	UDS	1.387	1.400	1.383	1.360	1.337	1.7
	LUDS	1.354	1.367	1.350	1.338	1.333	0.4
	MINMOD	1.349	1.371	1.349	1.339	1.335	0.3
2	UDS	1.546	1.443	1.318	1.219	1.120	8.8
	LUDS	1.308	1.222	[b]	[b]	–	–
	MINMOD	1.361	1.259	1.154	1.118	1.105	1.2
3	UDS	1.819	1.628	1.375	1.162	0.949	22.4
	LUDS	1.334	[b]	[b]	[b]	[b]	–
	MINMOD	1.517	1.266	1.014	0.946	0.923	2.5
4	UDS	2.074	1.845	1.526	1.203	0.880	36.7
	LUDS	1.378	[b]	[b]	[b]	[b]	–
	MINMOD	1.644	1.337	0.987	[c]	0.870	13.4
5	UDS	2.274	2.059	1.714	1.300	0.886	46.7
	LUDS	1.485	[b]	[b]	[b]	[b]	–
	MINMOD	1.687	1.517	1.127	[c]	0.997	13.0

[a] Calculated between Mesh 4 (or 3) and extrapolated values.
[b] Diverges.
[c] Convergence criterion not attained (solution oscillates).

complete. The use of a consistent mesh refinement technique allowed us to apply Richardson's extrapolation to the limit, using the values obtained with the three finest meshes, and the results for X_R and Ψ_R are presented in Tables 2 and 3. Table 3 also gives the lip vortex intensity within brackets. The data for X_R in Table 2 may be especially useful for benchmarking with this flow configuration since the uncertainty is quantified [25,31], being below 2.5% for De $\leq$ 3. For Ψ_R the extrapolation technique was applied only at low De numbers where the procedure produced reliable and physically realistic values. This limitation is due to the fact that evaluation of Ψ_R requires integration of the velocity field, and the order of the result is reduced by one (see Roache [31]). As a consequence, extrapolation of Ψ_R at high De numbers would require significantly more refined meshes in the contraction region, but this would entail a prohibitive calculation cost with the present method. This is even more clear for the quantification of the intensity of the lip vortex, and thus we decided not to extrapolate this latter quantity.

The simulations of Oliveira and Pinho [16] at a higher value of the Reynolds number (Re=1), for which inertial effects become important, show similar flow patterns to those obtained here (Fig. 7). It should be pointed out that such flow patterns, with the presence of lip vortices, have not been observed so far in reported visualisation studies of constant-viscosity fluids flowing through plane contractions, but have, on the other hand, been observed when shear-thinning or constant-viscosity fluids flow through

Table 3
Primary vortex intensity ($\Psi_R \times 10^3$) as a function of Deborah number, mesh and interpolating scheme[a]

De	Scheme	Mesh 1	Mesh 2	Mesh 3	Mesh 4	Extrapolated
0	CDS	1.209	1.185	1.164	1.161	1.160
	MINMOD	1.212	1.184	1.164	1.161	1.160
1	UDS	1.155 (0.439)	0.948 (0.241)	0.850 (0.124)	0.768 (0.051)	0.664
	LUDS	0.933 (0.384)	0.832 (0.210)	0.743 (0.136)	0.706 (0.102)	0.674
	MINMOD	0.913 (0.562)	0.813 (0.299)	0.741 (0.174)	0.707 (0.092)	0.674
2	UDS	2.401	1.400 (1.364)	0.794 (0.734)	0.527 (0.401)	0.284
	LUDS	0.963 (1.049)	0.563 (0.474)	[b]	[b]	–
	MINMOD	1.139 (1.384)	0.650 (1.116)	0.421 (0.403)	0.353 (0.390)	0.316
3	UDS	7.087	3.729 (4.234)	1.296 (2.149)	0.537 (1.030)	[d]
	LUDS	1.337 (1.429)	[b]	[b]	[b]	–
	MINMOD	2.687 (4.628)	0.886 (2.527)	0.285 (0.651)	0.205 (0.774)	0.192
4	UDS	12.294	8.678	4.276	0.911 (1.805)	[d]
	LUDS	2.355	[b]	[b]	[b]	–
	MINMOD	6.258	1.836 (3.630)	0.335 (1.623)	[c]	–
5	UDS	15.500	12.804	7.448	1.955	[d]
	LUDS	3.386	[b]	[b]	[b]	–
	MINMOD	6.793	6.361	1.006 (3.341)	[c]	–

[a] The values in brackets (when there is one) are for the lip vortex, $\Psi_{lip} \times 10^3$.

[b] Diverges.

[c] Convergence criterion not attained (solution oscilates).

[d] Negative (irrealistic) values.

axisymmetric contractions. Although not supported by the existing experimental evidence, the present findings are supported by the recent numerical simulations of Matallah et al. [9] and Xue et al. [30] who used FE and FV methods, respectively.

While some of the results of Oliveira and Pinho [7] are confirmed by the present study, others are quantitatively improved due to the higher accuracy of the MINMOD differencing scheme and the use of the very-fine Mesh 4. A summary of the main findings is now given.

- For Deborah numbers of 0 and 1 the previous results are confirmed with normalised vortex lengths of 1.50 and 1.34, respectively. The corner vortex strength predictions are more accurate now, and the extrapolated values of $\Psi_R \times 10^3$ become 1.16 and 0.67 (compared to values given in [7] of 1.14 and 0.63, respectively).
- As the Deborah number increases above 1, the lip vortex grows in size and strength, and the corner vortex diminishes, but more intensely than previously predicted. For De=2 and 3 we obtain now $X_R = 1.105$ and 0.923, respectively. Although the value at De=2 is close to the previously reported value of 1.19, at De=3 there is a qualitative difference in that now the vortex is seen to be still decreasing in size, whereas in [7] the vortex size was predicted to be already increasing (after the merging between corner and lip vortex had occurred). There is also a major improvement in the prediction of the vortex strength; while predictions with the UDS scheme gave irrealistic negative values of the extrapolated Ψ_R [7], the extrapolated values obtained here with MINMOD scheme are more realistic and accurate (see Table 3). Table 3 also includes the strength of the lip vortex (in brackets) and it is seen that for De ≥ 2 its intensity exceeds that of the corner vortex.
- For Deborah numbers above 3, the advantages of MINMOD over UDS are clearly visible. The results obtained with MINMOD in Mesh 3 are much closer to the extrapolated solution than the UDS results obtained in the very fine Mesh 4.

The influence of mesh refinement on the predicted flow pattern is illustrated by Fig. 8 which gives the streamlines predicted with the UDS and MINMOD schemes in Meshes 2–4, at De=3. The beneficial effects of the high-resolution scheme are again evident: the flow patterns in Meshes 3 and 4 show good convergence with mesh refinement for this moderately high Deborah number case. On the other hand, the first-order UDS scheme is unable to predict accurately the flow pattern even in the very fine Mesh 4 (although the extrapolated X_R value of 0.949 is close to the value of 0.923 obtained with MINMOD).

According to Roache [31], Richardson extrapolation applies not only to point-by-point solution values but also to solution functionals, provided that consistent or higher-order methods are used in their evaluation. It so happens that X_R for the contraction flow problem is a solution functional highly sensitive to mesh refinement, presumably due to the appearance of a lip vortex and interaction between the two (obviously, a too coarse grid will not resolve the lip vortex and the prediction of X_R and Ψ_R will be substantially different - much higher values will be obtained). The true order of accuracy of the method implemented in this work can thus be evaluated based on the recirculating length values X_R obtained in the finest three grids [31] yielding an order 1.9 very close to the theoretical value. Following Ferziger and Perić [25] and Roache [31] we can then use Richardson extrapolation of X_R as a means of quantitatively estimate the uncertainty of the numerical results and this is shown in Fig. 9 where the estimated error in X_R (predicted minus extrapolated values) is plotted in log-log scales as a function of the minimum mesh size, at the relatively high De=3. This figure not only demonstrates the second-order accuracy of the MINMOD scheme, in contrast with the first-order accuracy of the UDS scheme, but also reveals that MINMOD has achieved the asymptotic range in Mesh 2, for this De, whereas UDS shows signs

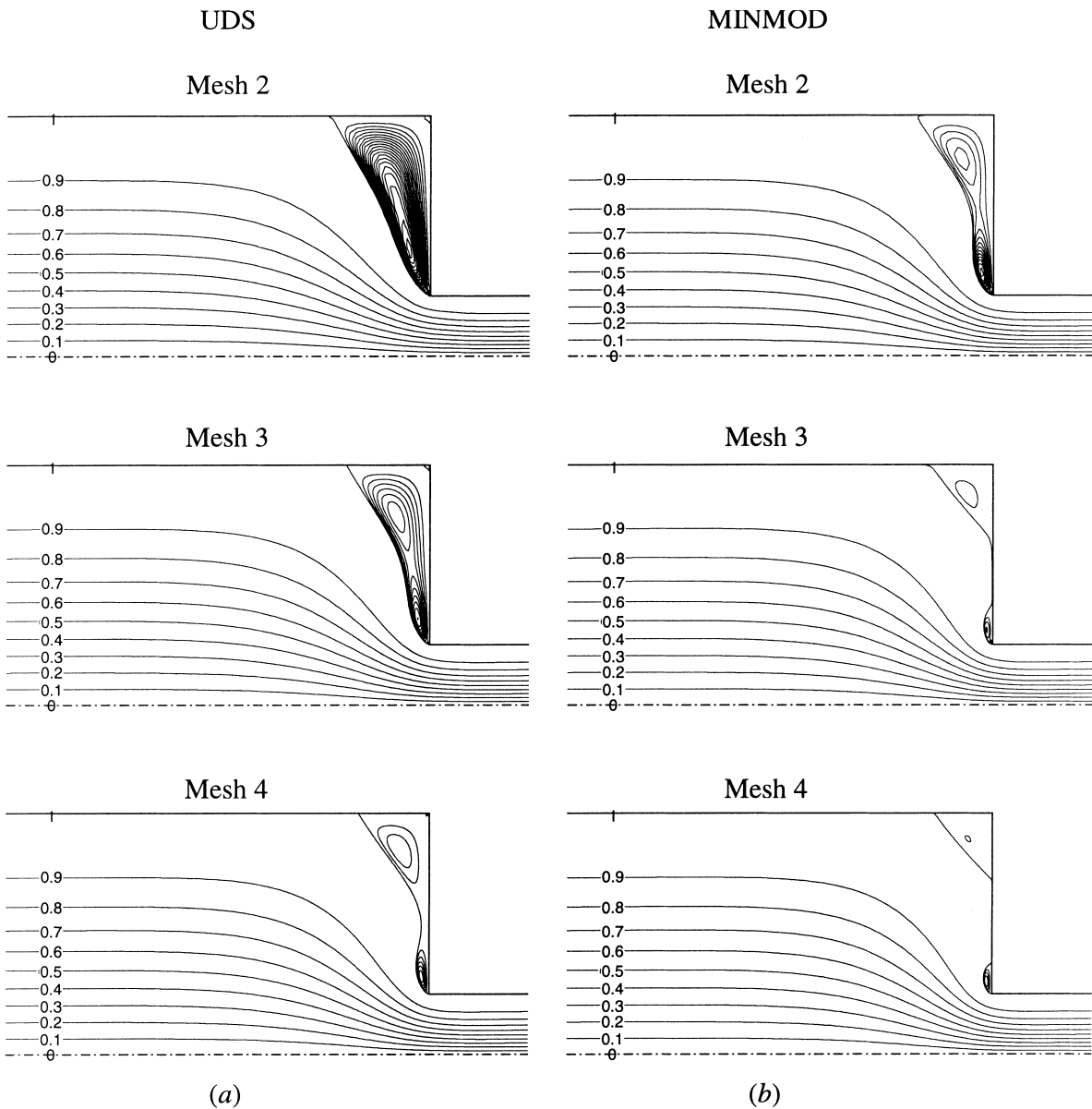UDS   MINMOD

Mesh 2   Mesh 2

Mesh 3   Mesh 3

Mesh 4   Mesh 4

(a)   (b)

Fig. 8. Coupled effect of mesh refinement and differencing scheme on the streamline patterns for Re=0.01 and De=3. (a) UDS scheme; (b) MINMOD scheme.

of approaching the asymptotic range only for meshes finer than Mesh 3. In order to better demonstrate these points we have decided to re-run the cases in Fig. 9 with three additional meshes which have mesh spacings in-between those of the base Meshes 1–4. The new points are included in Fig. 9 and corroborate the above assertions.
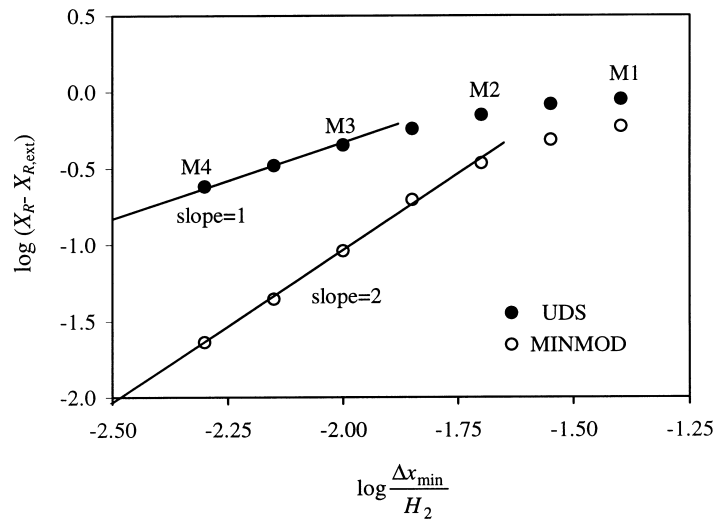
Fig. 9. Estimated error in X_R as a function of mesh refinement for the two differencing schemes at De=3.

5.3. Axial distribution of velocity, pressure and stresses along the centerline and near the downstream wall

In Fig. 10 the distribution of the streamwise velocity component, pressure and first normal stress difference are presented along the line $y/H_2 = 0.98$ for two cases: (a) De=0 and (b) De=3. The first normal stress difference ($N_1 = \tau_{xx} - \tau_{yy}$) is normalised with $T_w = 3\eta U_2/H_2$ and, as the figure shows, it is extremely sensitive to the mesh fineness along this line, which passes very close to the re-entrant corner singularity (at a normalised distance of 0.02). Even in the fine Mesh 3, N_1 is found to be somewhat different from the very fine Mesh 4 profile, for the flow case De=3. However, at lower De numbers the results are less sensitive to mesh refinement, as demonstrated in Fig. 10(a) for the Newtonian case. The streamwise velocity is much less sensitive to mesh refinement, although for De=3 there is still a slight deviation between the profiles predicted in the two fine meshes near the re-entrant corner (at $x/H_2 \approx 0$). We call attention to the enlarged x-scale in these plots (zooming the region around the singularity) designed to magnify possible differences among the results in the various meshes.

Stress behaviour near the singularity is further detailed in Figs. 11 and 12. Fig. 11 shows zoomed views of N_1 and pressure profiles at normalised y-positions gradually closer to the wall (distances of 0.0125, 0.075 and 0.0025), obtained in Mesh 4 at De=0 and De=3. The peaks in stress and pressure are seen to increase and become narrower as the singular point is approached. The evolution with position of the maximum first normal stress difference, near the singular point, is plotted in Fig. 12. In Fig. 12(a), the maximum N_1 at a given vertical position (y) is plotted against the normalised distance from the downstream wall, and the corresponding x-location is plotted against the same distance in Fig. 12(b). With mesh refinement, Fig. 12(a) shows the maximum N_1 increasing to infinity at the wall, and Fig. 12(b) shows that the point of maximum N_1 tends to the re-entrant corner position (x=0, $1-y/H_2$=0).
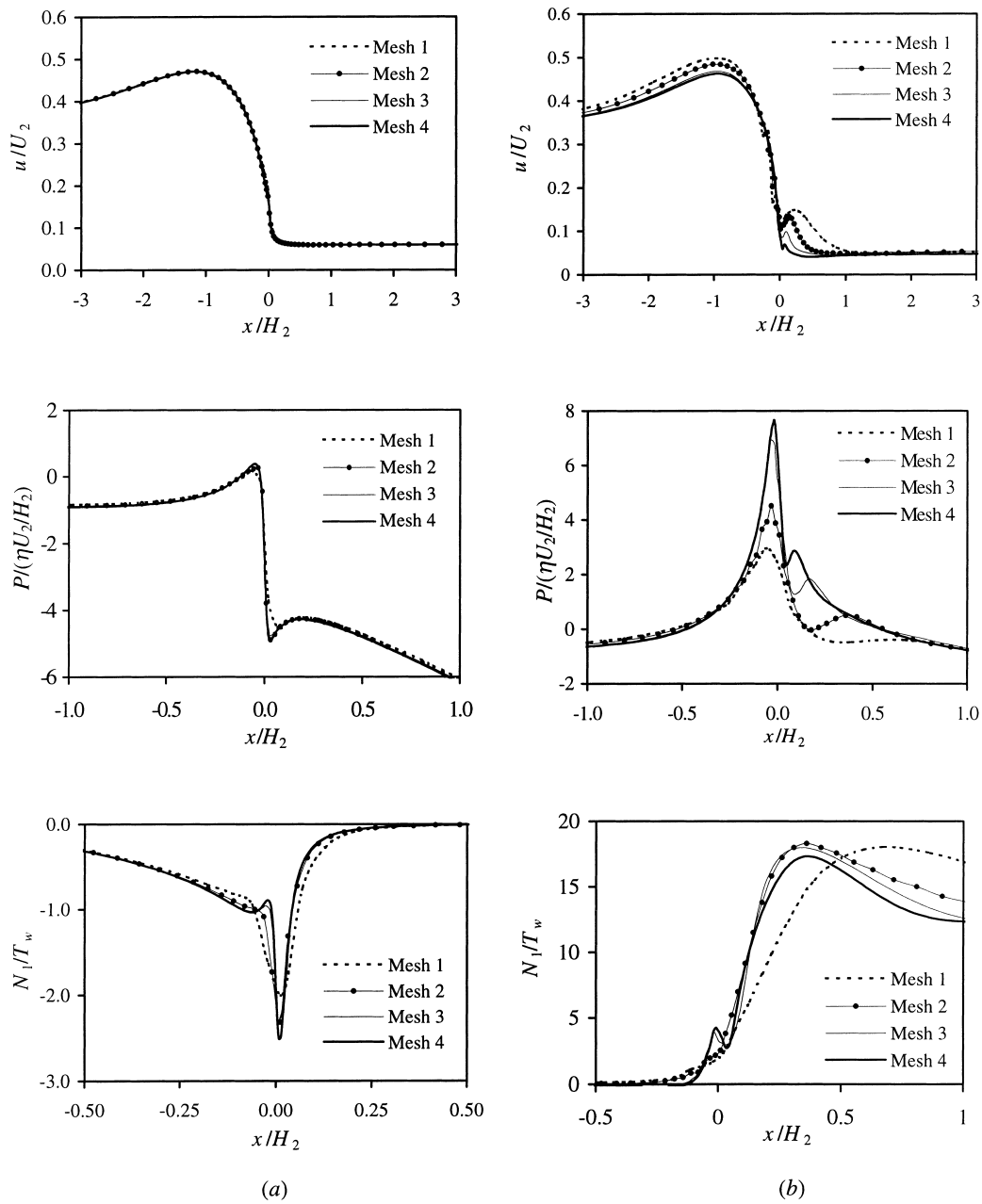
Fig. 10. Distributions along the line $y/H_2=0.98$ of predicted streamwise velocity, pressure and first normal stress difference for (a) De=0 and (b) De=3.

In Fig. 13, predicted profiles of longitudinal velocity, pressure and N_1 at the same Deborah numbers are presented along the centerline ($y/H_2 = 0$). As expected, the results are now much less sensitive to mesh refinement, and Mesh 3 is found to yield sufficiently accurate predictions of all variables, including N_1, for the Deborah number range in question.
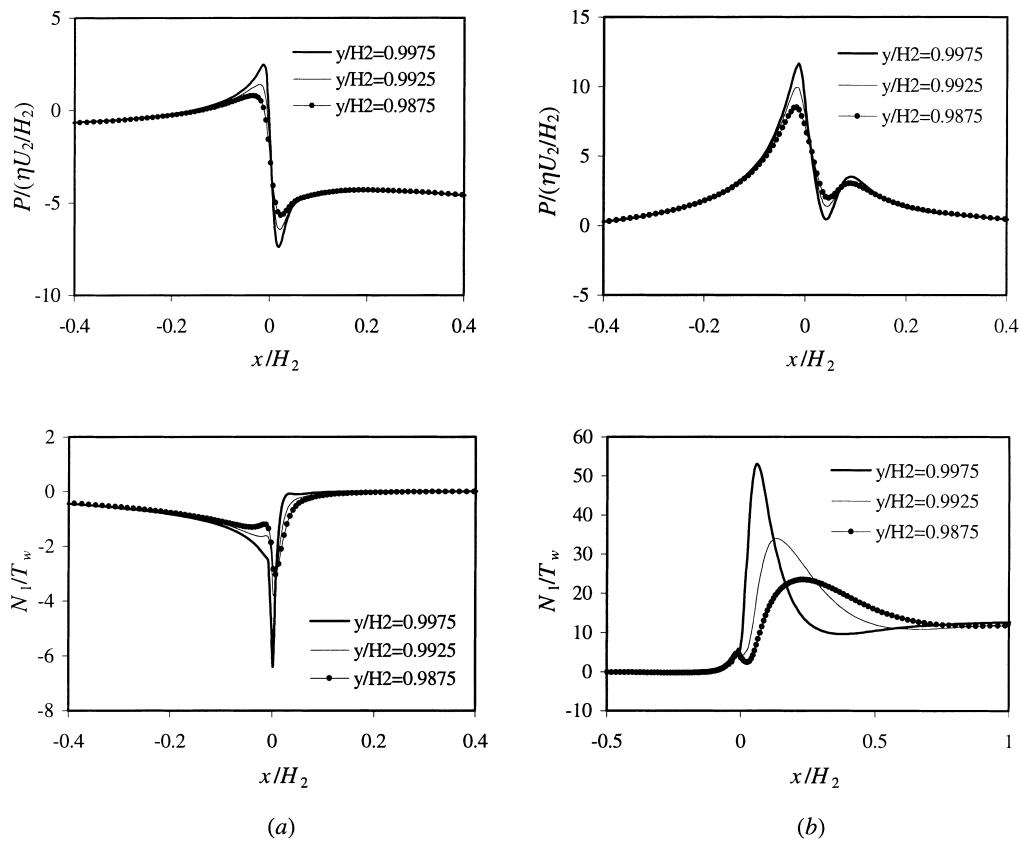
Fig. 11. Longitudinal distributions of pressure and first normal stress difference in the vicinity of the downstream wall and corner. Results obtained in Mesh 4 with MINMOD scheme at (a) De=0 and (b) De=3.

5.4. Stress fields near the singularity

Convergence with mesh refinement of the stress field is illustrated by Fig. 14 which shows contours of the first normal stress difference predicted on the three finest meshes at De=3. It is visually possible to detect the second-order accuracy of the method: as the typical mesh spacing is halved, going from Mesh 2 to 3, there is still some noticeable variation of the stress contours, but further halving of mesh spacing (Mesh 3 to 4) produces only a marginal variation, on the proportion 4:1 as expected from a second-order scheme ($O(h^2)$). The figure also shows that N_1 is smooth everywhere, even in the coarser Mesh 2. A detail of the region around the re-entrant corner is shown in Fig. 15, where contours are presented separately for the three stress components, for N_1 and for the pressure, at De=3, in Mesh 4. The maximum stresses are located on the downstream channel wall, very close to the re-entrant corner, and are then convected some distance downstream — memory effect in the constitutive equation. Again, the smoothness of the predicted stress fields near the singularity is noteworthy.
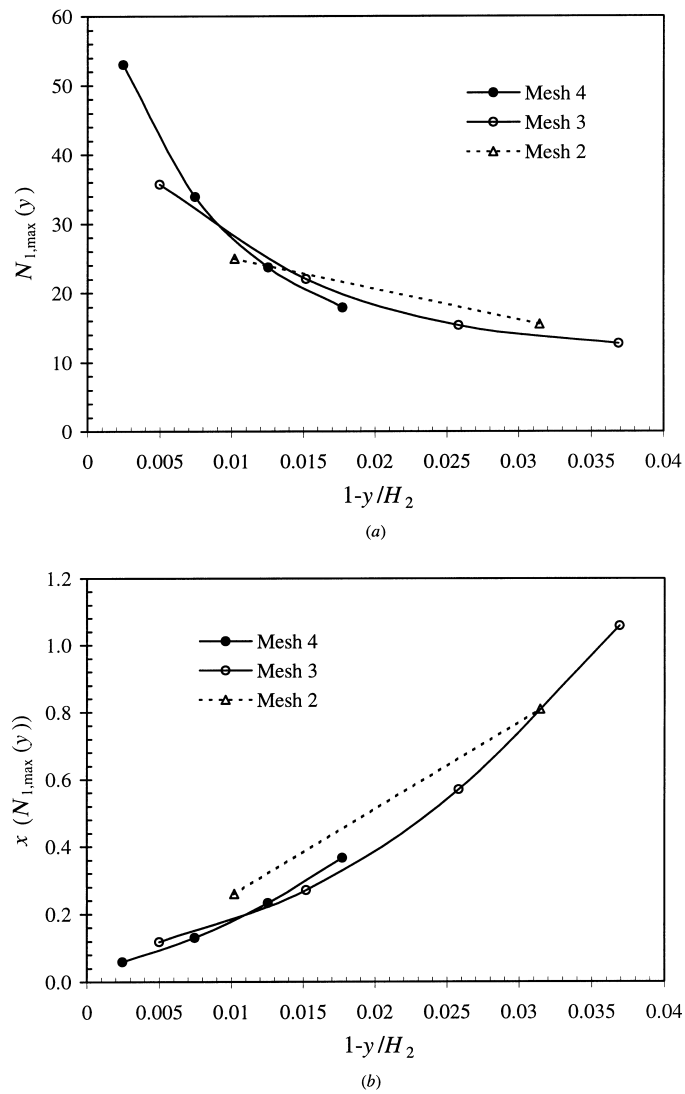
Fig. 12. (a) Variation of maximum N_1 with vertical distance from the downstream wall and (b) corresponding horizontal location. Results with MINMOD scheme at De=3.

## 5.5. Pressure drop through the contraction (Couette correction)

The pressure drop across the contraction is given in terms of a Couette correction [11]:

$$C = \frac{\Delta p - (\Delta p_1)_{\text{FD}} - (\Delta p_2)_{\text{FD}}}{2T_{\text{w}}}, \tag{34}$$

where Δp represents the pressure difference between the inlet and outlet planes, $(\Delta p_1)_{\text{FD}}$ and $(\Delta p_2)_{\text{FD}}$ are the pressure drops associated with fully developed flows in the upstream and downstream sections, respectively. The Couette correction values are given in Fig. 16, and good agreement is found between
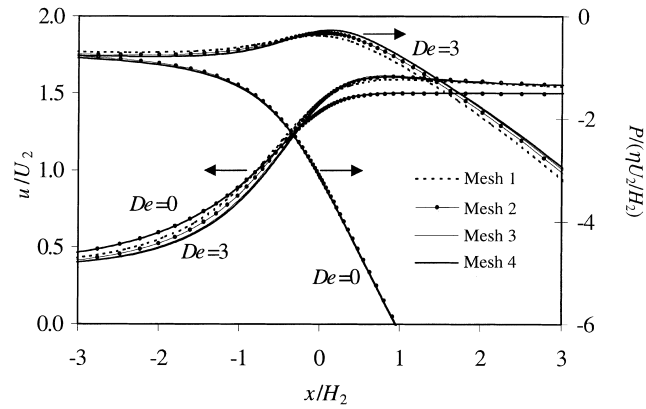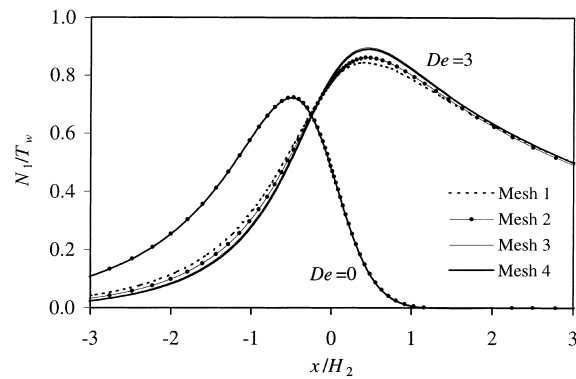
Fig. 13. Distributions along the centerline of (a) dimensionless streamwise velocity and pressure, and (b) first normal stress difference, for De=0 and De=3.
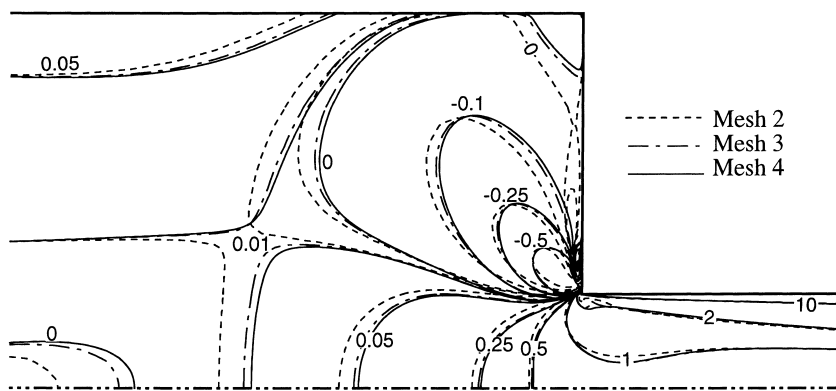

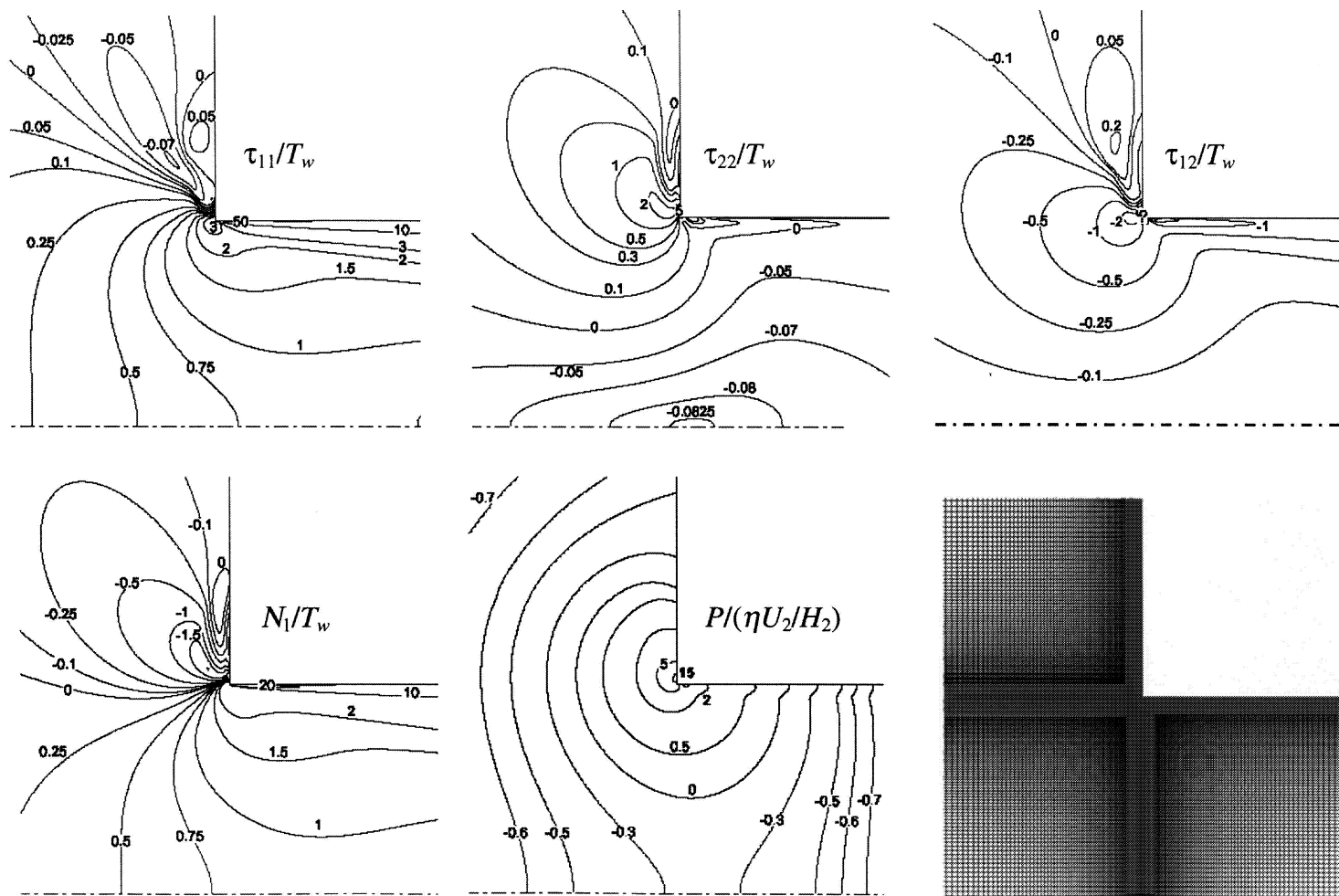Fig. 14. Contours of $N_1/(3\eta U_2/H_2)$ at De=3, obtained with the MINMOD scheme in Meshes 2–4.

Fig. 15. Contours of τ_{11}/T_w, τ_{22}/T_w, τ_{21}/T_w, N_1/T_w and $P/(\eta U_2/H_2)$ near the singularity, for De=3. The results were obtained with the MINMOD scheme in Mesh 4, which is also shown.
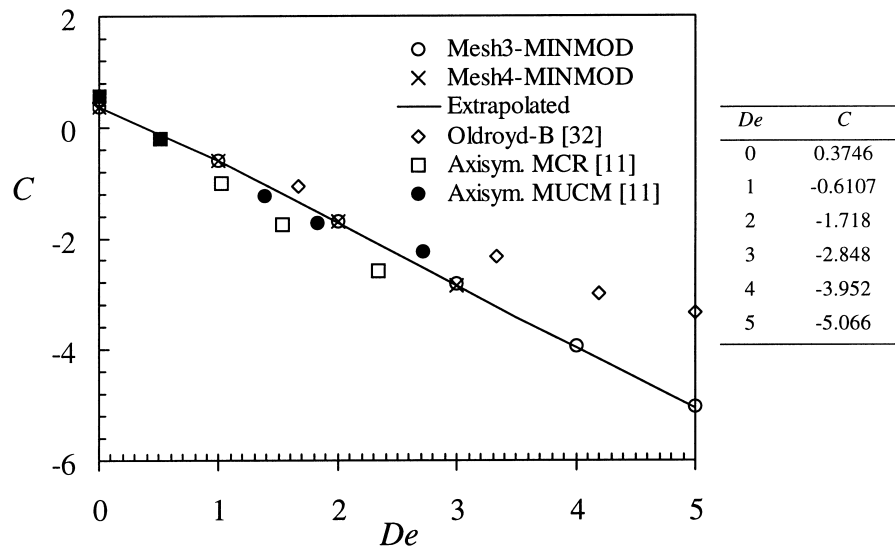
Fig. 16. Predicted values for the Couette correction.

the predictions in Meshes 3 and 4, and also with the extrapolated values, which are indistinguishable in the figure. The estimated accuracy of C, obtained from the relative difference between the extrapolated and finest mesh values, is 0.03% for the Newtonian case, 0.3% for De $\leq$ 3, and 0.7% for De $>$ 3.

To allow qualitative comparison with other related published data, we include in the figure the predictions of [11] in a 4:1 axisymmetric contraction with a modified UCM and modified Chilcott-Rallison models and those of [32] for the plane contraction of an Oldroyd-B fluid with $\lambda_2/\lambda_1 = 1/9$. We do not expected agreement due to different fluids and geometry, but the trend of variation of C with De is the same in all cases and the values are not too different. The higher values of C of [32], especially as De increases, may be due to the lower-order accuracy of their SU FEM method together with their coarse mesh.

6. Conclusions

The second-order LUDS and CDS cause convergence and stability limitations when applied to the finite-volume representation of the convective terms in the constitutive equation. In this work, these shortcomings have been alleviated by an adequate combination of both schemes so that the resulting high-resolution method (MINMOD) is forced to obey a strict convective boundedness criterion. The MINMOD scheme of Harten [13] was implemented and found to be approximately second-order accurate, enabling converged solutions of a UCM fluid in a 4:1 plane contraction. The estimated order of the scheme was found to be 1.9 based on a sensitive solution functional (the vortex size) predicted in three consecutively refined meshes in the asymptotic range.

Under creeping flow conditions (Re=0.01) solutions could be obtained up to a Deborah number of 5 in the fine Mesh 3 in contrast with a previous work [7] where solutions with the high-order linear-upwind and central-difference schemes were limited in that mesh to De=1 and 0, respectively. In an effort to

improve and to assess the accuracy of the results, an even finer mesh has been employed with a minimum normalised cell size of 0.005 near the re-entrant corner, and the MINMOD scheme was here able to provide converged solutions up to at least De=3. In our previous work, such high Deborah number values could only be reached with the first-order accurate upwind scheme and we are unaware of other finite-volume studies that make use of similarly refined meshes coupled with high-order schemes.

With the MINMOD scheme, the asymptotic behaviour of the velocity and stress fields of the UCM fluid near the singularity was found to be in good agreement with the theoretical predictions of Hinch [1]. The present simulations confirm the basic flow patterns predicted by Oliveira and Pinho [7] but are more accurate and thus provide better quantitative data for the vortex characteristics. As the Deborah number is increased, the lip vortex size and strength was found to increase, and the corner vortex to decrease. It is only when De=5 that the two vortices merge together, with the lip vortex still being dominant, and then start growing as a single remaining vortex.

The pressure drop coefficient (Couette correction) was predicted accurately up to De=5 and was found to decrease almost linearly with De, in agreement with other authors [11].

Acknowledgements

References

[1] E.J. Hinch, J. Non-Newtonian Fluid Mech. 50 (1993) 161–171.
[2] J.Y. Yoo, Y. Na, J. Non-Newtonian Fluid Mech. 39 (1991) 89–106.
[3] G.P. Sasmal, J. Non-Newtonian Fluid Mech. 56 (1995) 15–47.
[4] S.-C. Xue, N. Phan-Thien, R.I. Tanner, J. Non-Newtonian Fluid Mech. 59 (1995) 191–213.
[5] X. Huang, N. Phan-Thien, R.I. Tanner, J. Non-Newtonian Fluid Mech. 64 (1996) 71–92.
[6] P.J. Oliveira, F.T. Pinho, G.A. Pinto, J. Non-Newtonian Fluid Mech. 79 (1998) 1–43.
[7] P.J. Oliveira, F.T. Pinho, J. Non-Newtonian Fluid Mech. 88 (1999) 63–88.
[8] D. Rajagopalan, R.C. Armstrong, R.A. Brown, J. Non-Newtonian Fluid Mech. 36 (1990) 159–192.
[9] H. Matallah, P. Townsend, M.F. Webster, J. Non-Newtonian Fluid Mech. 75 (1998) 139–166.
[10] G. Mompean, M. Deville, J. Non-Newtonian Fluid Mech. 72 (1997) 253–279.
[11] P.J. Coates, R.C. Armstrong, R.A. Brown, J. Non-Newtonian Fluid Mech. 42 (1992) 141–188.
[12] P.H. Gaskell, A.K.C. Lau, Int. J. Numer. Methods Fluids 8 (1988) 617–641.
[13] A. Harten, J. Comput. Phys. 49 (1983) 357–393.
[14] M.S. Darwish, F. Moukalled, Numer. Heat Transfer Part B 26 (1994) 79–96.
[15] R.B. Bird, R.C. Armstrong, O. Hassager, Dynamics of Polymeric Liquids, 2nd Edition, Fluid Mechanics, Vol. 1, Wiley, 1987.
[16] P.J. Oliveira, F.T. Pinho, Numer. Heat Transfer Part B 35 (1999) 295–315.
[17] C.M. Rhie, W.L. Chow, AIAA J. 21 (11) (1983) 1525–1532.
[18] R.I. Issa, P.J. Oliveira, Comput. Fluids 23 (1994) 347–372.
[19] M.G.N. Perera, K. Walters, J. Non-Newtonian Fluid Mech. 2 (1977) 49–81.
[20] R. Guénette, M. Fortin, J. Non-Newtonian Fluid Mech. 60 (1995) 27–52.
[21] B.P. Leonard, S. Mokhtari, Int. J. Numer. Methods Eng. 30 (1990) 729–766.

[22] P.K. Khosla, S.G. Rubin, Comput. Fluids 2 (1974) 207–209.

[23] J.P. Van Doormal, G.D. Raithby, Numer. Heat Transfer 7 (1984) 147–163.

[24] J.A. Meijerink, H.A. Van der Vorst, Math. Comput. 31 (1977) 148–162.

[25] J.H. Ferziger, M. Perić, Int. J. Numer. Methods Fluids 23 (1996) 1263–1274.

[26] W.R. Dean, P.E. Montagnon, Proc. Cambr. Philos. Soc. 45 (1949) 389–394.

[27] H.K. Moffatt, J. Fluid Mech. 18 (1964) 1–18.

[28] F.P.T. Baaijens, J. Non-Newtonian Fluid Mech. 75 (1998) 119–138.

[29] M.R. Apelian, R.C. Armstrong, R.A. Brown, J. Non-Newtonian Fluid Mech. 27 (1988) 299–321.

[30] S.C. Xue, N. Phan-Thien, R.I. Tanner, J. Non-Newtonian Fluid Mech. 74 (1998) 195–245.

[31] P.J. Roache, Annu. Rev. Fluid Mech. 29 (1997) 123–160.

[32] B. Debbaut, J.M. Marchal, M.J. Crochet, J. Non-Newtonian Fluid Mech. 29 (1988) 119–146.